Non-Destructive and Non-Invasive Approaches for the Identification of Hydroxy Lead–Calcium Phosphate Solid Solutions ((Pb x Ca 1– x) 5 (PO 4) 3 OH) in Cultural Heritage Materials

Claudio Costantino, Letizia Monico, Francesca Rosi, Riccardo Vivani, Aldo Romani, Luis Carlos Colocho Hurtarte, Eduardo Villalobos-Portillo, Christoph Sahle, Thomas Huthwelker, Catherine Dejoie, et al.

Non-destructive and Non-invasive Approaches for the Identification of Hydroxy Lead-Calcium Phosphate Solid Solutions [$(Pb_xCa_{1-x})_5(PO_4)_3OH$] in Cultural Heritage Materials

Claudio Costantino[1,2], Letizia Monico[2,1,3,*], Francesca Rosi[2], Riccardo Vivani[4], Aldo Romani[1,2,*], Luis Carlos Colocho Hurtarte[5‡], Eduardo Villalobos-Portillo[5‖], Christoph J. Sahle[5], Thomas Huthwelker[6], Catherine Dejoie[5], Manfred Burghammer[5], Marine Cotte[5,7,*]

[1] *Centre of Excellence SMAArt and Department of Chemistry, Biology and Biotechnology, University of Perugia, Via Elce di Sotto 8, 06123 Perugia (Italy)*

[2] *CNR-SCITEC, c/o Department of Chemistry, Biology and Biotechnology, University of Perugia, Via Elce di Sotto 8, 06123 Perugia (Italy)*

[3] *AXIS Research Group, NANOlab Centre of Excellence, Department of Physics, University of Antwerp, Groenenborgerlaan 171, 2020, Antwerp, Belgium*

[4] *Pharmaceutical Science Department, University of Perugia, Via Elce di Sotto 8, 06123 Perugia (Italy)*

[5] *European Synchrotron Radiation Facility, Avenue des Martyrs 71, 38000 Grenoble (France)*

[6] *Swiss Light Source, Paul Scherrer Institut, Forschungsstrasse 111, 5232 Villigen PSI (Switzerland)*

[7] *Sorbonne Université, CNRS, Laboratoire d'archéologie moléculaire et structurale, LAMS, UMR 8220, 75005 Paris (France)*

[‡] *present address: Diamond Light Source, Diamond House, Harwell Science and Innovation Campus, Fermi Ave, Didcot OX11 0DE (United Kingdom)*

[‖] *present address: ALBA Synchrotron, Carrer de la Llum 2-26, 08290 Cerdanyola del Vallès, Barcelona (Spain)*

Corresponding authors:

Letizia Monico: letizia.monico@cnr.it;

Aldo Romani: aldo.romani@unipg.it;

Marine Cotte: marine.cotte@esrf.fr

Abstract

Lead-calcium phosphates are unusual compounds sometimes found in different kinds of cultural heritage objects.

Structural and physico-chemical properties of this family of materials [who fall in to the hydroxypyromorphite-hydroxyapatite solid solution, $(Pb_xCa_{1-x})_5(PO_4)_3OH$] have received considerable attention during the last decades for promising applications in different fields of environmental and material sciences, but their diagnostic implications in the cultural heritage context have been poorly explored.

This paper aims at providing a clearer understanding of the relationship between compositional and structural properties of the peculiar series of $(Pb_xCa_{1-x})_5(PO_4)_3OH$ solid solutions and at determining key markers for their proper non-destructive and non-invasive identification in cultural heritage samples and objects.

For this purpose, a systematic study of powders and paint mock-ups made up of commercial and in-house synthesized $(Pb_xCa_{1-x})_5(PO_4)_3OH$ compounds with a different Pb^{2+}/Ca^{2+} ratio was carried out via a multi-technique approach based on scanning electron microscopy (SEM), synchrotron radiation-based X-ray techniques [i.e. X-ray powder diffraction (XRPD) and X-ray absorption near edge structure (XANES) spectroscopy at the Ca K- and P K-edges] and vibrational spectroscopy methods [i.e., micro-Raman and Fourier Transform Infrared (FT-IR) spectroscopy].

The spectral modifications observed in the hydroxypyromorphite-hydroxyapatite solid solution series are discussed, by assessing advantages and disadvantages of the proposed techniques and by providing reference data and optimized approaches for future non-destructive and non-invasive applications to study cultural heritage objects and samples.

Introduction

An unusual lead compound has recently been detected in red and black inks from a corpus of Egyptian papyri belonging to Rome's Imperial period (ca. 100 to 200 CE).[1]

Synchrotron radiation (SR)-based micro-X-ray fluorescence (μ-XRF) mapping combined with micro-X-ray powder diffraction (μ-XRPD) showed that crystalline lead calcium phosphorus-containing compounds are present in several of such inks. While the detection of XPb_2Cl_5 ($X=K^+$ or NH_4^+) was ascribed to some degradation processes, as it leads to a whitening of the original reddish and black colors of the ink, the origin and exact chemical formula of lead calcium phosphorus-based compounds is still unclear. Earlier studies report the presence of lead (calcium) phosphates in different archaeological and artistic contexts, but their origin is still a matter of debate.[2–6] The identification of hydroxypyromorphite [$Pb_5(PO_4)_3OH$; hereinafter called “HPy”] in red ochre paints of certain Roman wall paintings, could be related to the use of sandyx, a pigment prepared by mixing pyromorphite [$Pb_5(PO_4)_3Cl$] and red ochre, as described by Pliny the Elder (ca. 23 CE to 79 CE).[7] The use of pyromorphite as a whitening pigment has also been reported and suggested in Early Islamic artworks at Nishapur, north-eastern Iran, where the importation of such mineral was hypothesized.[8] Lead phosphate [$Pb_9(PO_4)_6$], found in a 14th century Japanese Buddhist painting on silk is thought to have been used as a white pigment.[9] Other studies, carried out in artistic contexts, have ascribed lead phosphates to degradation, namely: (i) the result of specific interactions between the metallic alloy of a buried Roman bronze inkwell and residues from agricultural fertilizers and soil amendments;[4] (ii) the interaction of lead from bronze with contiguous phosphate-based material (bone or ivory) of a dining table of the Han dynasty;[5] (iii) the reaction of hydroxyapatite [$Ca_5(PO_4)_3OH$; hereinafter referred to as “HA”] with litharge (tetragonal PbO), cerussite ($PbCO_3$) or other lead oxides in tools employed for the preparation or use of lead-containing pigments at Akrotiri (Thera, Greece) during the Early-Middle Greek Bronze Age (ca. 3000–1600 BCE).[6]

In such a context, the role played by HA while reacting with lead compounds might be significant, by involving its well-known high cationic substitution capacity.[10] This property is notably exploited, for example, for the decontamination of heavy metals, including Pb^{2+}, in polluted environments.[11–13] Pb^{2+} can partially substitute Ca^{2+} within the HA crystal, thus forming a solid solution series, $(Pb_xCa_{1-x})_5(PO_4)_3OH$ (with $0 < x < 1$; henceforth called PbHA-X). It is reasonable to assume that such (a partial) substitution process might be one of the main pathways for the formation of lead-calcium phosphate compounds in artistic materials.

Based on what is mentioned above, it becomes relevant to assess the presence and distribution of different types of lead-calcium phosphate solid solutions in complex matrices as part of the manufacture history of heritage objects and of their proper conservation and public display. Also, the increased use of phosphate solutions for the consolidation and conservation of calcium-based cultural heritage materials is a further motivation to better understand the nature, formation, and stability of these materials.[14]

Within this framework, the present research aims at (i) extending our knowledge about the relationship between compositional and structural properties of the PbHA-X compounds and (ii) determining key markers for the identification of the PbHA-X solid solution series allowing the proper non-destructive and non-invasive characterization primarily in cultural heritage samples and objects.

For this purpose, the systematic study of eight powders and over fifteen paint mock-ups made up of commercial and in-house synthesized PbHA-X compounds was performed through an integrated multi-technique approach based on scanning electron microscopy (SEM), SR-based X-ray techniques [i.e., XRPD and X-ray absorption near edge structure (XANES) spectroscopy at the Ca K- and P K-edges] and vibrational spectroscopy methods [i.e., μ-Raman and Fourier Transform Infrared (FT-IR)]. The efficiency of these vibrational techniques for the potential study of cultural heritage objects and corresponding samples was also assessed through the analysis of paint mock-ups made up of commercial and in-house synthesized powders applied as pictorial layers using two different binding media, namely linseed oil and arabic gum.

Materials and Methods

Synthesis of PbHA-X compounds and preparation of paint mock-ups

The synthesis of a series of PbHA-X compounds [where X is the $Pb^{2+}/(Pb^{2+}+Ca^{2+})$ molar ratio in the synthesis solution multiplied by 100] was performed according to earlier literature.[15] A set of solutions containing a variable $Pb^{2+}/(Pb^{2+}+Ca^{2+})$ molar ratio (equal to 0 and 1, in HA and HPy, respectively) were prepared by dissolving in distilled water different amounts of $Pb(CH_3COO)_2$ and $Ca(CH_3COO)_2 \cdot 3H_2O$, with the total amount of lead and calcium in each solution being maintained at 0.4 mol/L. The solutions were then mixed with a CH_3COONH_4 buffer solution (4.4 mol/L). Then, a 0.12 mol/L solution of $NH_4H_2PO_4$ was quickly added to the previous solution under stirring and the pH was adjusted to circa 7.50 with an NH_3 30% (w/w) solution. After the pH adjustment, the resulting solution was left for 10 min under stirring at room temperature, thus aged at 100°C for 48h, and the obtained precipitate was carefully washed with distilled water and dried in an oven at 70°C overnight. The complete list of the analyzed commercial and in-house synthesized powders along with the corresponding XRPD results is reported in Table I.

Two different sets of paint mock-ups were prepared by employing either cold-pressed linseed oil or arabic gum as binding media (both by Zecchi, Italy). Oil paint mock-ups were obtained by mixing either HA (Sigma-Aldrich, Germany) or PbHA-X or HPy (in-house synthesized) in a variable powder:binder weight ratio (1:1, for HA; ca. 2:1 for PbHA-X solid solutions; 4:1 for HPy), in order to obtain a paintable mixture. Arabic gum paints were instead prepared by mixing the same powders in a powder:binder weight ratio of about 1:1.

All mixtures obtained were then applied on polycarbonate slices and left to dry for about two months at environmental temperature (~35 °C) and relative humidity percentage (RH ~35-40%) before being analyzed.

Analytical Methods

In what follows, a comprehensive description of the analytical methods employed for the analysis of HA, HPy, PbHA-X powders and corresponding paint mock-ups is provided.

SEM analysis

SEM analysis was used to observe the particle shape and size of powders. Morphological images were recorded by the Field Emission Gun – Scanning Electron Microscope (FEG-SEM) LEO 1525 (ZEISS) based on the third-generation GEMINI column. The microscope operated at 20 kV acceleration voltage with a nominal resolution of 1.5 nm. All the secondary electron images were acquired by a high-efficiency in-lens detector. Each sample was allocated on a stub and metalized with carbon.

XRPD analysis

Different XRPD instruments were used to characterize the powders. First, a laboratory setup (Lab-XRPD) was used for a primary characterization of powders. Second, the SR high-angular resolution powder X-ray diffraction (HR-XRPD) setup was employed for the precise determination of the

crystallographic structures, the crystallite size, and microstrain. Third, SR μ-XRPD maps were acquired using a micrometric beam to assess the future detection of such compounds in complex, multi-layer historical cultural heritage samples.

Lab-XRPD patterns were collected with the Ni-filtered CuKα radiation on a PANalytical X'PERT PRO diffractometer, PW3050 goniometer equipped with an X'Celerator detector. The long fine focus (LFF) ceramic tube operated at 40 kV and 40 mA. Data were collected in the 7°-140° 2θ range, using a 0.017° step scan and 800 s counting time. Microcrystalline silicon, in a weighted amount, was added as an internal standard to correctly refine unit cell parameters. To minimize preferred orientations of microcrystals, samples were carefully ground on an agate mortar and then side-loaded onto an aluminum sample holder with an oriented quartz monocrystal underneath.

SR HR-XRPD and μ-XRPD were carried out at the ID22 beamline and ID13 beamline, respectively, at the European Synchrotron Radiation Facility (ESRF, Grenoble), benefitting from the Historical Materials Block Allocation Group (BAG) access.[16-18]

At ID22, HR-XRPD measurements were performed using a 13-channel Si (111) multi-analyzer stage and with an incident beam energy of 35.0 keV (0.354205 Å) and of 1×1 mm^2 size. The 300-500 μm glass capillaries, filled with powder, were spun at 991 rpm during the experiment to avoid preferred orientation effects. Data were collected in the 0.002°-41.912° 2θ range and combined into 0.002° bins for further treatments. The wavelength of incident radiation and the goniometer alignment were calibrated using the pattern of Si (NIST SRM640), while the instrumental resolution function, that is the contribution of the instrumental parameters to the peak profile as a function of 2θ, could be obtained by the analysis of a pattern of LaB_6 (NIST SRM 660).

At beamline ID13, μ-XRPD data were acquired by spreading each powder as a thin layer on a Kapton® tape, covered with an Ultralene® film. Samples were mounted vertically, perpendicular to the micro-beam. The energy of the incident beam was 13.0 keV (0.953734 Å). The beam was focused down to ~2×2 $μm^2$ using compound refractive lenses mounted in a transfocator. μ-XRPD maps were obtained by raster scanning the samples in air and collecting XRPD 2D patterns, in transmission, with a DECTRIS EIGER 4M single photon counting detector that provides frames with 2070×2167 pixels (75×75 $μm^2$ pixel size) at a rate up to 750 Hz. μ-XRPD maps were acquired with a dwell time of 25 ms/pixel. 2D XRPD patterns were azimuthally integrated using the PyFAI software package[19] through dedicated Jupyter notebooks.[19,20] This creates .h5 files with an integrated XRPD pattern of each pixel of the 2D maps. μ-XRPD maps were analyzed with the PyMca ROI imaging software package.[21] Average XRPD patterns were calculated over the entire map.

The lab-XRPD, HR-XRPD patterns, and some of the μ-XRPD average patterns were fitted by Rietveld refinements following the structural models obtained from the literature and using the GSAS-II software package.[22] The refinement involved the scale factor, background, unit cell, peak profile parameters, atomic positions, and isotropic displacement factors. Site occupancy factors of Ca and Pb atoms, which share the same crystallographic sites, were also refined. At the end of the

refinement procedure, the calculated shifts of all refined parameters were less than their estimated standard deviations.

XANES at P K- and Ca K-edges

Ca and P K-edge XANES analyses were performed in unfocussed mode at the beamline ID21 of the ESRF.[23] The beam size was set to 0.2-0.3 mm^2 using slits. Powders were glued on tape and covered with an Ultralene® foil. The samples were mounted vertically, with an angle of 62° with respect to the incident beam. The X-ray energy of the incoming beam was selected and tuned by means of a horizontal deflecting double-mirror system (Si coating for higher harmonics rejection) and a Si (111) monochromator ($\Delta E/E \sim 2.10^{-4}$). The beam intensity was monitored continuously using a photodiode placed upstream of the sample. XANES spectra were acquired both in transmission and in XRF mode. XRF was measured using a large area (80 mm^2 collimated active area) Silicon Drift Diode (Bruker, Karlsruhe, Germany). For these measurements, two regions of interest were defined over Ca and P Kα X-ray emission lines. The transmission was simultaneously measured by a photodiode placed downstream of the sample.

XANES spectra were acquired via the graphical user interface Daiquiri,[24] by scanning the energy from 2.14 to 2.2 keV with steps of 0.20 eV at the P K-edge, and from 4.02 to 4.11 keV with steps of 0.24 eV at the Ca K-edge. The monochromator was calibrated using HA (maximum of absorption at 2152.7 eV) at the P K-edge and $CaCO_3$ (maximum of absorption at 4050 eV) at the Ca K-edge. The slight peak energy shifts observed in the XANES spectra with respect to those earlier reported reflect differences in monochromator calibrations.[25]

Mid and near FT-IR spectroscopy

A portable ALPHA spectrophotometer (Bruker Optics, Germany/USA) was used to perform transmission and external reflection mode mid FT-IR measurements of powders and paint mock-ups, respectively. The instrument is equipped with a Globar source, a DLaTGS detector, and a modified Michelson interferometer (RockSolid™). A dedicated module was employed for transmission mode measurements of powders diluted on KBr pellets, that were prepared by mixing a few mg of each sample in ca. 120 mg of KBr powder. Data were recorded in the 4000–320 cm^{-1} spectral range, with 2 cm^{-1} spectral resolution, and with 200 scans. Deconvolution of transmission mode FT-IR spectra was performed by means of the Origin 2018 software, using a Gaussian curve fitting. The curve-fit results were characterized by squared regression coefficient values $R^2 \geq 0.992$ (Figure S1, Supplemental Material).

A reflectance module was employed to non-invasively acquire pseudo-absorbance spectra [A'=log(1/R), with R=reflectance] directly at the surface of paint mock-ups with an optical layout of 22°/22°. Profiles were recorded from areas of 6 mm diameter, in the 7000–320 cm^{-1} range, with 4 cm^{-1} spectral resolution, and with 800 scans. Background was performed from a gold mirror plate.

Non-invasive reflectance near FT-IR measurements were performed on paint mock-ups using a portable JASCO VIR-9600 spectrophotometer equipped with a fiber optic sampling probe. The

optical bench top consists of a halogen lamp as the source, a Michelson interferometer equipped with a CaF_2 beam splitter, and a room-temperature InGaAs detector. Spectra were recorded in the 15000–4000 cm^{-1} spectral range, with 4 cm^{-1} spectral resolution, and with 800-1000 scans. During measurements, the fiber optic probe was kept perpendicular to the sample surface, by allowing the reflection from an area of ca. 10 mm^2 to be measured. The background was acquired on a metal mirror plate.

Raman spectroscopy

μ-Raman investigations of powders were carried out by means of a bench-top JASCO NRS-3100 double-grating spectrophotometer connected to an optical microscope with a confocal setup (100× objective) and equipped with a charge-coupled device detector cooled down to −47 °C. Analysis were performed using a 785 nm (diode laser) excitation wavelength with power values between 0.5 and 14.5 mW and a 600 lines/mm grating. Spectra were collected in the 1850–200 cm^{-1} wavenumber range, the exposure time varied between 3 and 40 s, with 3–30 accumulations and with a spectral resolution of ca. 5-6 cm^{-1}. The curve-fit of the spectra was carried out via Origin 2018 using Lorentzian functions as components. The curve-fit results were characterized by squared regression coefficient values $R^2 \geq 0.973$ (Figure S2, Supplemental Material).

To evaluate the possibility of non-invasively identifying different PbHA-X compounds in situ and non-invasively on artworks, additional tests were performed on paint mock-ups by employing a portable Raman instrument verifying any potential laser-induced damage at the surface of the paint. Spectra were recorded by means of a B&W Tec Exemplar® T spectrophotometer equipped with an optical fiber (diameter of 105 μm) that focuses the laser radiation into an optical microscope (20× objective). The backscattered Raman light was collected by a second optical fiber (diameter of 200 μm) and led to a 2048-element High Quantum Efficiency Back-Thinned CCD Array detector kept at -2° C by a thermoelectric cooler. The maximum laser power at the sample was ca. 25 mW and 0.6 mW for the 785 and 532 nm excitations, respectively. The exposure time varied between 1 s and 10 s, using 1-15 accumulations. The spectral resolution was ca. 5 cm^{-1}. To be noted that, under these acquisition conditions, no visible laser radiation damage of the paint surface nor spectral modifications were observed during and after exposure at the maximum power of both lasers (namely: ca. 250 mW at 785 nm and about 40 mW at 532 nm).

Results

To identify suitable analytical markers for the discrimination of different PbHA-X compounds, in a first step, we investigated the effects of the Pb content in the morphological, microstructural, and local atomic structure of PbHA-X by SEM, XRPD, and XANES at Ca K- and P K-edges. In a second step, further information on the molecular structure of these materials was obtained by vibrational spectroscopy. The feasibility of potentially identifying and distinguishing non-invasively different PbHA-X materials on historical artworks was also assessed by exploiting FT-IR and Raman portable devices. Results are described and discussed hereafter.

Morphological and microstructural characterization by SEM and XRPD

SEM images recorded from HA, PbHA-X and HPy compounds (Figure S3, Supplemental Material) show that all samples are made of crystallites with homogeneous shape and size, approximately in the 20-100 nm range. The shape of the crystallites is rather isotropic for all powders, except for HA PbHA-10 and PbHA-20, for which one dimension appears somewhat longer than the others, and HPy that appears made up of thin platelets.

Such visual observations were determined more accurately by the refinement of the average size of coherent crystallinity domains (or crystallite size, indicated as Dv) and lattice defects and deformations (or microstrain, indicated as a percentage of deformation, ε) with the Rietveld procedure against ID22 HR-XRPD data (Table I).[26] Calculations of both parameters were performed by adopting either isotropic or uniaxial models. The isotropic model assumes a spherical parameter distribution to describe, which only one value is needed. The uniaxial model describes instead the distribution of the values of the microstructural parameters along two directions, parallel and perpendicular to a given crystallographic axis, in this case the (0 0 1) axis. For as concern the crystallite size parameter, the uniaxial model was adopted for those samples showing a marked morphological anisotropy by SEM imaging, namely, HA, PbHA-10, PbHA-20, and HPy. For these samples the statistical agreement factors (Rp and Rwp) were significantly improved by the adoption of the uniaxial model and the refined values obtained were in general agreement with the SEM analysis. The remaining samples were satisfactorily described by isotropic size models. For what concerns microstrain, for all samples the introduction of anisotropic effects did not significantly improve the refinement, therefore an isotropic model was adopted. Rietveld plots for all powders are reported in Figure S4 (Supplemental Material).

Table I. Composition (x), unit cell parameters, crystallite size (Dv) and % isotropic microstrain (ε) values for $(Pb_xCa_{1-x})_5(PO_4)_3OH$ ($0 \leq x \leq 1$) powders obtained by Rietveld refinement procedures with ID22 HR-XRPD data. Values in brackets indicate the error associated with the analysis.

Sample	x	a (Å)	c (Å)	Dv⊥ (nm)[(a)]	Dv|| (nm)[(a)]	ε (%)
HA	0	9.4261(6)	6.8699(1)	25(1)	118(1)	0.31(1)
PbHA-10	0.112(1)	9.4776(5)	6.9115(1)	26(1)	83(1)	0.36(1)
PbHA-20	0.286(1)	9.5654(7)	6.9730(1)	22(1)	65(1)	0.83(1)
PbHA-40	0.453(2)	9.6356(9)	7.0434(2)	38(1)[(b)]	-	2.2(1)
PbHA-50	0.530(1)	9.681(1)	7.0981(2)	31(1)[(b)]	-	2.0(1)
PbHA-70	0.733(5)	9.761(1)	7.2443(2)	46(1)[(b)]	-	2.0(1)
PbHA-80	0.769 (2)	9.7927(6)	7.3067(2)	54(1)[(b)]	-	1.3(1)
HPy	1	9.8797(6)	7.4148(1)	32(1)	103(1)	0.58(1)

[(a)] Dv⊥ and Dv|| perpendicular and parallel to the (0 0 1) crystallographic axis, respectively; [(b)] average isotropic Dv.

All samples were described with a structural model derived from that of the pure HA hexagonal symmetry, space group $P6_3/m$.[27] PbHA-X samples were considered as solid solutions, in which Pb atoms isomorphously replace Ca atoms in their two crystallographically independent positions in the HA structure. Therefore, Ca1 and Pb1 occupy a 4f Wyckhoff position, with a coordination number of 9, which corresponds to an estimated ionic radius of 1.18 and 1.35 Å, respectively; Ca2 and Pb2 occupy instead a 6h position, with a coordination number of 7 and ionic radius of 1.06 and 1.23 Å, respectively. In both coordinations, the difference in the estimated Ca and Pb ionic radii is 0.17 Å. When Pb replaces Ca, this difference induces a linear increase with the exchanged fraction of average unit cell parameters (Vegard's law). However, as reported earlier,[28] Pb has a strong preference for the 6h position, probably because it is less hindered than 4f. It follows that the 4f position starts to be massively exchanged only when the 6h position is almost fully exchanged, which occurs for about a 50% global exchange. Notably, in the samples described here, for a global replacement of 53%, the 6h position is 79% occupied by Pb, while the 4f position is only 14% exchanged. The refined site occupancy factors for all samples are reported in Table S1. The replacement of Ca with Pb in 4f position induces a larger increase in the *c* lattice parameter than the same replacement in 6h because their reciprocal distances are shorter along the c axis (~3.43 Å) than other directions (~3.95 Å) and other crystallographic sites (~4.16 Å). For these reasons, the plot of the c axis vs x_{Pb} shows two distinct linear trends (Figure 1a, red): the range $0 < x_{Pb} < 0.5$ mainly refers to the exchange of the 6h position, while the range $0.5 < x < 1$ mainly refers to the exchange of the 4f position. The plot of the lattice parameter a vs x_{Pb} is instead described only by one linear regression equation (Figure 1a, black). These results highlight that the composition of a specific PbHA-X compound in heterogeneous and complex cultural heritage samples (but also soil samples), is in principle feasible only based on the position of a few diffraction peaks.

Pb content of powders HA, PbHA-X and HPy was also obtained by Inductively Coupled Plasma-Optical Emission Spectrometry (ICP-OES) and the results are in general good agreement with those obtained via Rietveld method refinement and Vegard's law (Table S1, Supplemental Material).

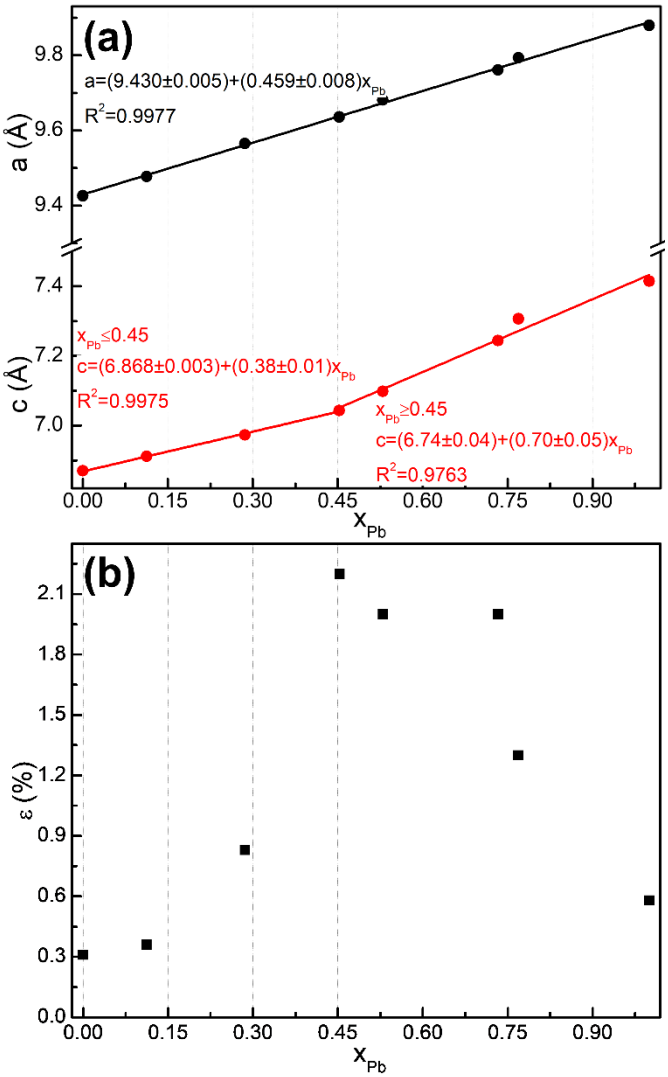

Figure 1. (a) Unit cell parameters and (b) % microstrain (ε) as a function of lead content for $(Pb_xCa_{1-x})_5(PO_4)_3OH$ ($0 \le x \le 1$) powders. Crystallographic parameters were obtained by Rietveld refinements of ID22 HR-XRPD data (cf. Table I).

Furthermore, the replacement of Ca with Pb induces a local distortion (or microstrain) of the crystal lattice, which can be estimated by the analysis of XRPD patterns. Crystallite size and microstrain are the most relevant factors that usually contribute to the broadening of diffraction peak profiles. By the refinement of the peak profiles as a function of 2θ in a sufficiently wide region, it is possible to separate and estimate the size and microstrain of the sample: the peak broadening depends on size effects with 1/cos θ, while microstrain contribution depends on tan θ. In some cases, it is possible to estimate also the anisotropic size and microstrain, because they affect to a different extent distinct classes of diffraction peaks. The results obtained about size agree with what is visualized in the SEM images (Figure S3, Supplemental Material). The microstrain level shows a characteristic dependence on x_{Pb}: it is limited for the lowest and highest values, while it is more pronounced for intermediate values (~0.45), when the massive occupation of 6h positions by the Pb ions starts to occur (Figure 1b). This suggests that the end-term HA and HPy structures easily accept a low level of defects represented by the replacement of a small amount of Ca with Pb, and Pb with Ca,

respectively. When, instead, 4h positions are almost completely occupied by Pb, the introduction of additional Pb ions in the 6h positions causes the largest structural distortions.

It should be noted that, due to relatively small crystallite sizes and high microstrain levels, the broadening of PbHA-X patterns is rather high and can be detectable even by lower resolution set-ups as the μ-XRPD of the ID13 beamline and the lab XRPD system (Figure S5, Supplemental Material).

Local atomic structure by XANES spectroscopy

The P K-edge XANES spectra of HA, PbHA-X and HPy powders are shown in Figure 2a-c. The position of the K absorption edge ranges from ~2152 to 2153 eV and is attributed to a dipole allowed transition K of a 1s core electron to 3p-dominant unoccupied states. Across the samples, the energy position of the white line increases with increasing lead content from 2152.7 to 2154 eV (Figure 2a), while the intensity decreases (Figure S6a). The spectra of samples with higher Pb content ($x_{Pb} > 0.4$) show a distinct pre-edge feature in the energy range 2148–2151 eV (Figure 2b). Such a result is consistent with the one earlier described for phosphate minerals by Ingall et al.[29] The characteristic post-edge shoulder of calcium phosphates at 2155.5 eV gradually disappears with increasing Pb content (Figure 2c).[29,30] Another post-edge peak at 2163 eV is visible in the spectrum of HA, decreasing its energy position to ca. 2160 eV for HPy with increasing Pb content.

Ca K-edge XANES spectra from the same set of lead phosphate samples are shown in Figure 2d,f. The XANES spectra result from the excitation of Ca 1s electrons to empty molecular orbitals localized on the calcium atom. More specifically, the spectral features in the pre-edge region (Figure 2e) are attributed to the transition of a 1s core electron to the 3d molecular orbital, which may include both quadrupole (1s → 3d) and dipole allowed (1s → 3d + np) transitions.[31] In addition, the position of the white line decreases with increasing Pb content from ~4050 to ~4048 eV (Figure 2d), while the intensity decreases (Figure S6b). Furthermore, the pre-edge region of the Ca XANES spectra, which is routinely used to assess the Ca coordination environment,[31] shows a decreasing intensity with increasing Pb content (Figure 2e). This can be explained by the fact that Ca2 is characterized by a local structure that is more distorted than that of Ca1. With increasing Pb content, the amount of Ca2 decreases, the symmetry increases, the transition 1s→3d is less allowed and the pre-edge peak intensity decreases. The post-edge band located between 4050 and 4052 eV also shows a slight modification with changing Pb content (Figure 2f).

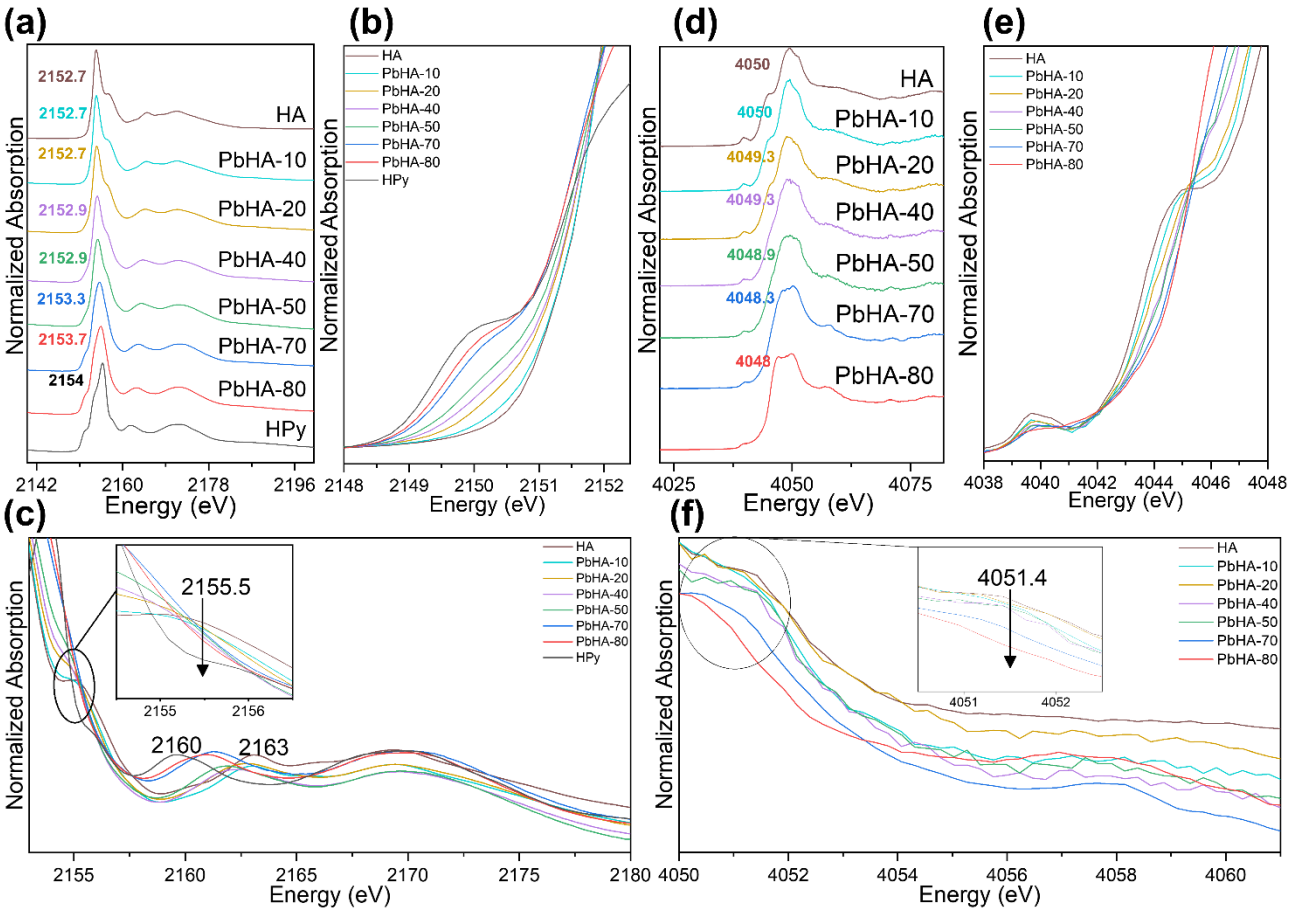

Figure 2. XANES spectra at (a) P K-edge and (d) Ca K-edge of $(Pb_xCa_{1-x})_5(PO_4)_3OH$ ($0 \leq x \leq 1$) powders and corresponding close-up views of (b, f) pre-edge and (c, f) post-edge regions. Insets in (c, f) show the spectral energy range as highlighted by circles.

Additional measurements by High Energy Resolution Fluorescence Detected (HERFD) XANES spectroscopy at the $K\alpha_1$ emission of phosphorus were also performed. Despite a lower background than conventional XANES, HERFD-XANES spectra did not improve (or only slightly increase/improved) the informational gain (Figures S7 and S8, Supplemental Material).

Based on what is described above, the band-shape and energy position of pre-/post-edge signals and of the white line of the XANES spectra at the P K-edge and Ca K-edge can be used as markers for the non-destructive discrimination of different PbHA-X compounds at the micro-scale length.

Molecular structure by vibrational spectroscopy

The transmission mode FT-IR and μ-Raman spectra of HA, PbHA-X, and HPy powders are reported in Figure 3. Two main different regions assigned to the vibrational modes of the tetrahedral PO_4^{3-} group are visible: that of the stretching modes (symmetric: v_1 and asymmetric: v_3) and one of the bending modes (symmetric: v_2 and asymmetric: v_4).[32] Molecular group theory, site symmetry, and factor group treatments explain the splitting of vibrational modes of the PO_4^{3-} group and why some of its symmetric and antisymmetric modes become IR active and Raman active, respectively.[33]

As widely described in the literature,[34–37] the v_3 modes of HA (brown line) are detectable at 1092 and 1045 cm^{-1} in the FT-IR spectrum, whereas they are located as weak Raman bands at 1077, 1046, and 1030 cm^{-1}.

The strong v_1 mode is recognizable at 962 cm^{-1} in the Raman spectra and as a weaker band at 960 cm^{-1} in the corresponding FT-IR profiles.[38–40] The IR v_4 and v_2 bending modes are present at 602, 568 cm^{-1} and 472 cm^{-1}, while the corresponding Raman bands are visible at 609, 591, 579, 448 and 430 cm^{-1}.[41–43] Bands of the hydroxyl group are located at 3566 and 633 cm^{-1} and are assigned to the stretching [v(OH)] and libration modes [v_l(OH)], respectively.[38,39] As reported earlier for a series of synthetic substituted hydroxyapatite compounds,[15,44–47] the position and band-shape of peaks depend on the nature of the incorporated cation and the extent of substitution. Vibrational spectra of PbHA-X solid solutions and HPy clearly show a shift of all PO_4^{3-} peaks towards lower wavenumbers and a change of their band-shape with increasing Pb amount. A lower wavenumber shift is observed also for the v(OH) mode (from 3566 to 3555 cm^{-1}), whose intensity is altogether lower when Pb^{2+} cations are present in the apatite lattice. Noteworthy, the position of this band is different from that of other basic carbonates used as pigments (e.g., hydrocerussite, v(OH) at ca. 3535 cm^{-1}).[48]

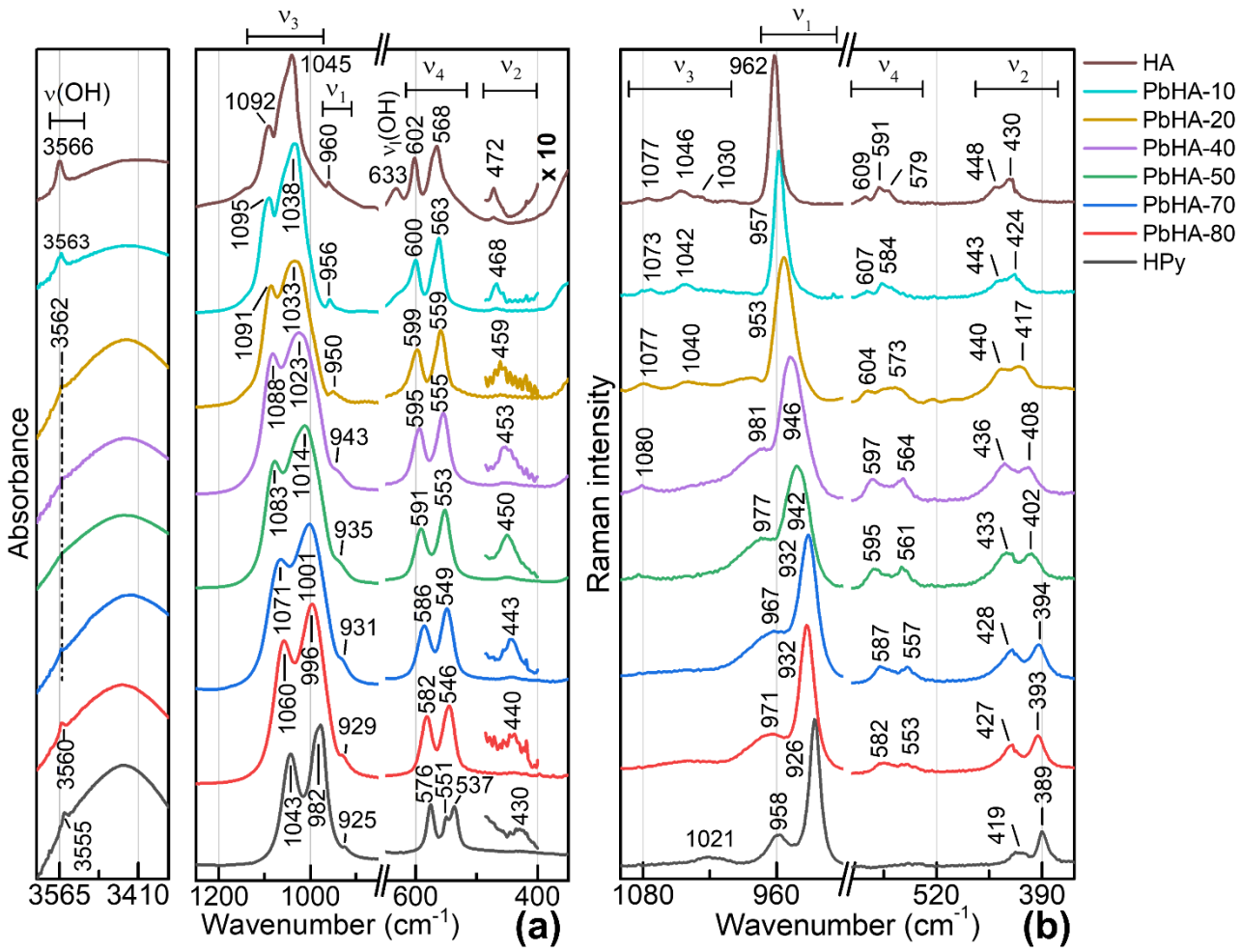

Figure 3. (a) Transmission mode FT-IR and (b) μ-Raman (λ_{exc}=785 nm) spectra of $(Pb_xCa_{1-x})_5(PO_4)_3OH$ ($0 \leq x \leq 1$) powders.

To find reliable spectral markers for distinguishing different PbHA-X compounds, the band component analysis was applied to the P–O stretching (v_1/v_3) and bending (v_2/v_4) regions of the vibrational spectra (Figures S1 and S2, Supplemental Material). Overall, consistent with XRD results (Figure 1a and Table I), the substitution of lighter Ca^{2+} ions with heavier Pb^{2+} ions, that leads to the hydroxyapatite lattice expansion, is the main responsible for the changes observed in the position, shape, width, and intensity of v_1/v_3 and v_2/v_4 bands. Notably, the wavenumber positions of the most intense IR (v_3 and v_4) and Raman (v_1 and v_2) modes monotonically decrease with increasing lead content (Figure 4a,b). The full widths at half maximum (FWHM) of both v_3 and v_1 bands (Figure 4c,d) show a discontinuity, by reaching a maximum value at x_{Pb} of ca. 0.4-0.5 and then progressively decreasing again until the Ca^{2+} substitution with Pb^{2+} is complete (i.e., x_{Pb}=1). In addition, the intensity of symmetric and antisymmetric stretching/bending modes of PO_4^{3-} group decreases with increasing Pb content in IR and Raman spectra, respectively.

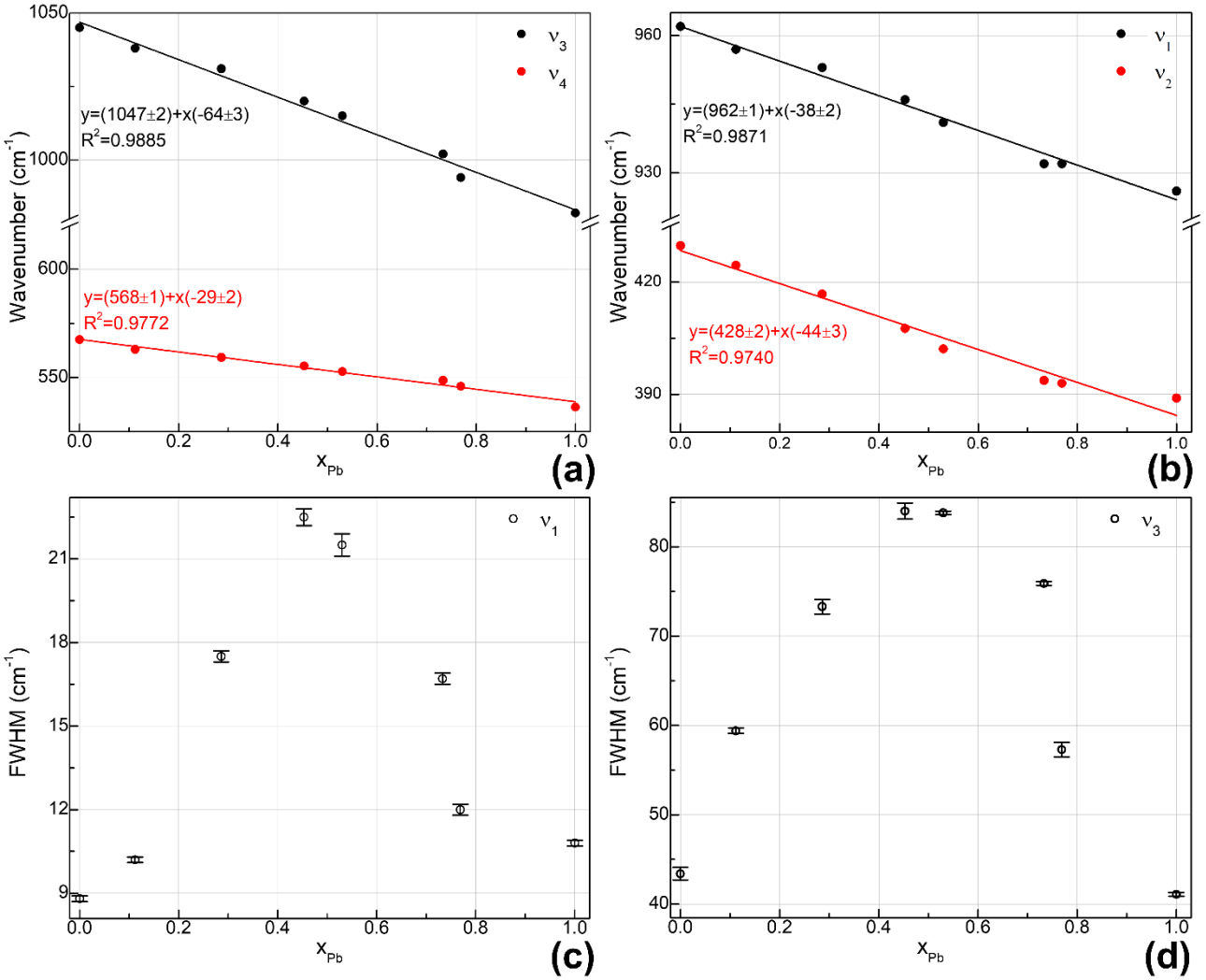

Figure 4. Wavenumber band positions of (a) $v_3(PO_4^{3-})$ (black) and $v_4(PO_4^{3-})$ (red) IR modes and (b) $v_1(PO_4^{3-})$ (black) and $v_2(PO_4^{3-})$ (red) Raman modes versus the lead content obtained via Rietveld refinement of XRPD patterns and corresponding results of the linear fit for $(Pb_xCa_{1-x})_5(PO_4)_3OH$ powders. Full width at half maximum (FWHM) values of (c) $v_3(PO_4^{3-})$ and (D) $v_1(PO_4^{3-})$ bands versus the lead content obtained via Rietveld refinement of XRPD patterns (See Figures S1 and S2 for further information about the results of the band component analysis).

Discrimination by non-invasive vibrational spectroscopy

To establish the feasibility of non-invasively and in situ detecting, without any sampling, different PbHA-X compounds directly at the surface of cultural heritage objects, arabic gum and linseed oil paint mock-ups were also examined by external reflection FT-IR and Raman spectroscopy by employing portable devices. As earlier reported for different kinds of artworks,[48-52] the study via non-invasive external reflection modality of a set of reference materials is a fundamental step for improving the interpretation of datasets recorded in a similar manner from historical objects because it permits to: (i) enhance knowledge about the type of spectral distortion occurring in the mid-IR range (visible as changes in the shape-band and position of the fundamental vibrational modes); (ii) assess any presence of combination/overtone bands in the near-IR wavenumber range, usually too weak to be detected in transmission mode working on samples/powders.

Reflection mode near FT-IR spectra in the 7200–6500 cm^{-1} range are shown in Figure 5a. The strong feature located in this range is due to the first overtones of the fundamental hydroxyl stretching modes [2v(OH)] showing approximately a doubling of the wavenumber shift observed for the fundamental mode at 3566-3555 cm^{-1} (Figure 3a).[53] For both gum and oil paint mock-ups, the band shift is of 6 cm^{-1} from HA (6973 cm^{-1}) to PbHA-50 (6979 cm^{-1}), while it becomes significant for x_{Pb}>0.5, undergoing a progressive red-shift up until about 20 cm^{-1} for HPy (6954 cm^{-1}). A decrease of the intensity and a broadening of the 2v(OH) mode is observed going from HA to PbHA-50; for x_{Pb}>0.5 an opposite trend is instead detected. It should be noted that for the arabic gum mock-ups, the 2v(OH) band is not visible in PbHA-40 and PbHA-50 samples, this is possibly due to the contribution of the signal of the binding medium in the same region (*cf.* light grey line in Figure 5a and Figure S9, Supplemental Material, for the spectra recorded from pure powders). Between 6500 and 4000 cm^{-1} only signals from the binding medium are observable (spectral range not shown).

Moving toward the mid-IR region (Figure 5b), all paint mock-ups, as expected, highlight the presence of spectral distortions (if compared to transmittance spectra of Figure 3a), with significant changes occurring in band maximum position, shape, and relative intensity due to a combined/unpredictable contribution of both surface and volume components of the reflected light linked to the optical properties of the paint.[54] Generally, $v_3(PO_4^{3-})$ modes appear inverted due to a *reststrahlen* effect, related to the surface reflected light in correspondence of the high absorption index values (k>1) of the P-O stretching bands; $v_4(PO_4^{3-})$ modes show instead an almost derivative-like profiles, the latter effect dominated by dispersion as ruled by Fresnel reflection for k<1.[49,50,54]

Despite these spectral distortions and consistent with transmission mode mid-FTIR results (cf. Figure 3a), a progressive shift towards lower wavenumbers is still observable in the minima and inflections points of $v_3/v_4(PO_4^{3-})$ peaks with increasing Pb amount, thus allowing a reliable distinction among different PbHA-X materials to be performed, even in the presence of the binders (Figure 5c). The minor differences that are visible in the band-shape, relative intensity, and position of v_3/v_4 (PO_4^{3-}) modes of the spectra recorded from oil and gum paint mock-ups may be imputable to

the variable contribution of the two binding media in this spectral region,[55] in addition to the already mentioned spectral distortions due to the surface optical properties.

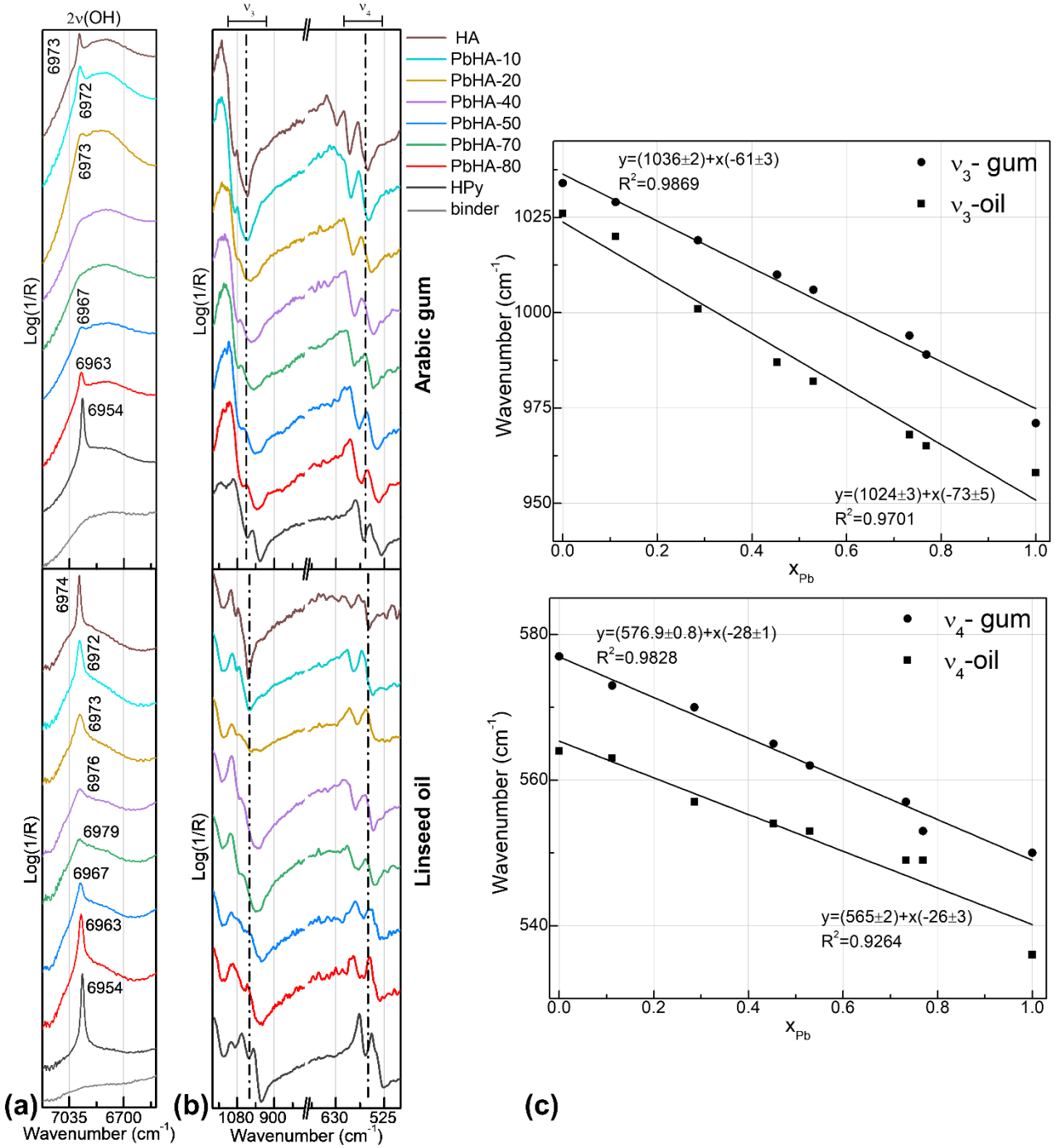

Figure 5. Non-invasive external reflection IR spectroscopy of arabic gum (top) and linseed oil (bottom) paint mock-ups containing different types of $(Pb_xCa_{1-x})_5(PO_4)_3OH$ powders: (a) near-FT-IR spectra, (b) mid FT-IR spectra. (c) Wavenumber band positions (minimum and inflection point) of $\nu_3(PO_4^{3-})$ (top) and $\nu_4(PO_4^{3-})$ (bottom) reflection IR modes of the $(Pb_xCa_{1-x})_5(PO_4)_3OH$ series painted with arabic gum (circle) and linseed oil (square) versus the lead content obtained via Rietveld refinement of XRPD patterns and corresponding results of the linear fit.

As done for FT-IR spectroscopy, data from paint mock-ups were collected by a portable Raman spectrometer (Figure 6). With respect to the equivalent spectra recorded from powders with the bench-top instrument, also equipped with a confocal set up at 785 nm (Figure 3b), the higher fluorescence background, due to the presence of the binding medium (even more significant for oil paint mock-ups), makes difficult/impossible the detection of the v_2 and $v_4(PO_4^{3-})$ modes. Nevertheless, analogous systematic differences to those of powders can be observed in the position of the $v_1(PO_4^{3-})$ band as a function of the Pb content. It follows that this signal can be used as a reliable marker for the non-invasive discrimination of different PbHA-X compounds in cultural heritage objects. Regarding measurements performed at 532 nm (results not shown), Raman signals were all masked by a strong fluorescence background, therefore indicating 785 nm excitation as the most appropriate wavelength for the non-invasive Raman detection and discrimination of HA, PbHA-X solid solutions and HPy in oil and gum painted historical artworks.

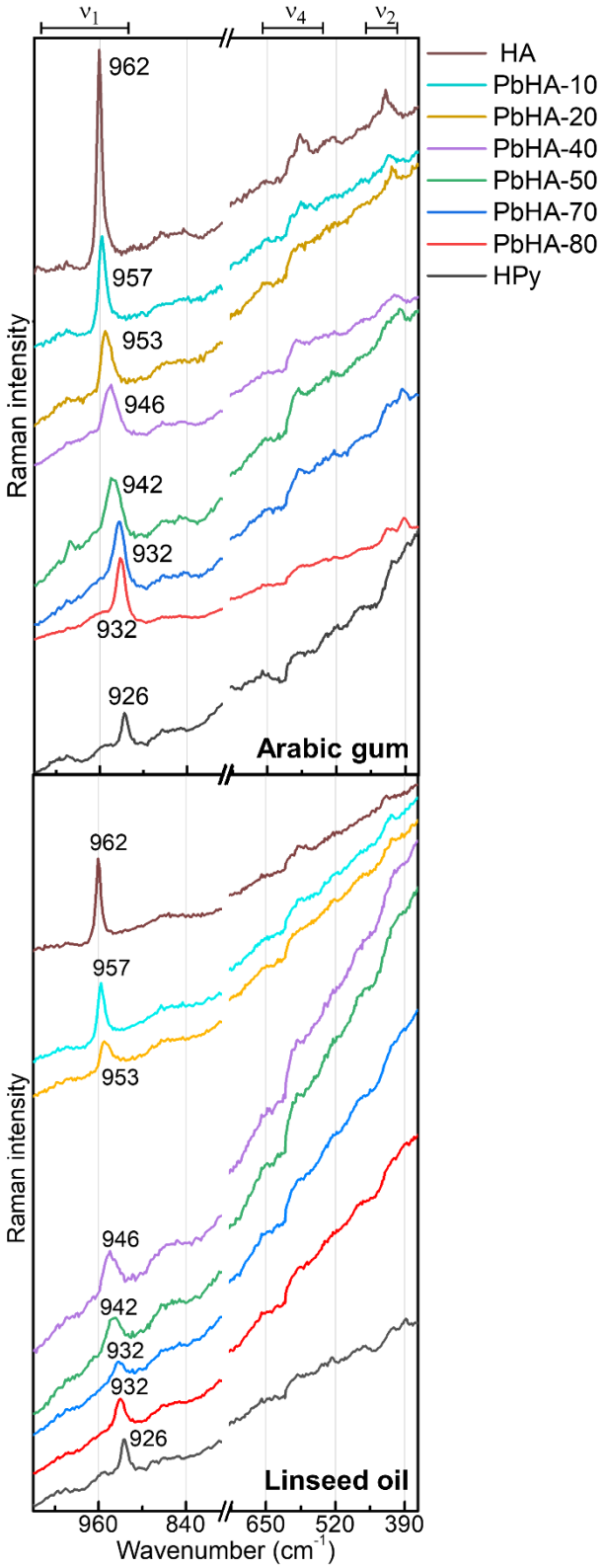

Figure 6. Raman spectra of arabic gum (top) and linseed oil (bottom) paint mock-ups containing $(Pb_xCa_{1-x})_5(PO_4)_3OH$ ($0 \leq x \leq 1$) acquired by the portable device (λ_{exc}=785 nm).

Discussion and conclusion

The dual aim of the present paper was to expand the knowledge on the PbHA-X solid solution series as well as determining key markers for their identification and localization at both the micro- and macro-scale lengths either on available micro-samples or directly in situ through non-destructive and non-invasive approaches, respectively.

Both aims were achieved by applying different XRPD setups (employing both synchrotron radiation and traditional sources) and via the use of X-ray absorption and vibrational spectroscopies.

A detailed description of the crystallographic properties was achieved by comparing data collected using different XRPD systems, providing a precise phase refinement of the unit cell and composition parameters, as well as microstructural information (i.e., crystallite size and microstrain) along the solid solution series. Diffraction peak positions and microstrain levels show a characteristic dependence with the solid solution composition. Such information can be clearly determined either with HR-XRPD measurements at the ESRF-ID22 beamline, but also with the μ-XRPD mapping set-up at ESRF-ID13 beamline, and even with the laboratory diffractometer, despite the lower angular resolution of both systems. Nevertheless, the possibility of performing μ-XRPD mapping at the microscale and HR XRPD bulk measurements is a clear added value for the study of available historical fragments, given their compositional heterogeneity. Based on these results and the state-of-the-art instrumental performances of available portable XRPD systems,[56,57] the non-invasive identification and localization of different PbHA-X solid solutions is likely already achievable also by in situ XRPD mapping at the macro-scale length.

XANES spectroscopy at P K- and Ca K-edges offers further markers for the discrimination of different types of PbHA-X compounds. Considering the capability of such a technique to detect both crystalline and amorphous phases and the possibility of working with sub-micrometric beams (in mapping and single point modes) at different synchrotron facilities (including ESRF-ID21 beamline), it can be used in a complementary fashion to SR μ-XRPD mapping for the analysis of minute samples, including those obtained from cultural heritage objects.

In PbHA-X solid solutions, the substitution of Ca^{2+} ions by larger Pb^{2+} ions lead to a volume increase of the hexagonal unit cell. Such changes are linked to a different extent to the main fundamental vibrational bands of these materials. Notably, the phosphate stretching (v_1/v_3) and the bending multiplet (v_2/v_4) are significantly influenced by the Ca^{2+}/Pb^{2+} substitution, showing a shift of band positions and modification of band shapes/widths as a function of the cell expansion namely the solid solution composition. The compositional dependence of these key markers is also exploited by using portable instrumentations applied to laboratory mock-ups with a more complex and heterogeneous composition to mimic real artworks. The obtained results open the possibility to non-invasively detect and distinguish in situ different types of PbHA-X compounds directly from the artwork itself.

Overall, the outcomes of the present study form the basis of a database that is expected to contribute to interpret more accurately data already available or of new acquisition from objects on

which the co-localized presence of Pb, Ca, and P have been identified. Beyond artistic materials, this work might also open relevant possibilities for future applications in environmental science, considering the widespread interest in hydroxyapatite-like compounds in this field.[10–13]

Furthermore, since the presence of phosphohedyphane ($Ca_2Pb_3(PO_4)_3Cl$) and hydroxy-chlorapatites solid solutions with a variable Cl^- content and Ca^{2+}/Pb^{2+}substitution has been reported in Roman carbon blacks and other historical objects, respectively,[1,4,5,8,9,58] it will be relevant to extend this study to similar phases. Additional experiments are also required to understand if and how such compounds can form in historical samples, notably which are the original lead-, calcium- and phosphorus-based materials.

Funding

The research at CNR-SCITEC and University of Perugia was financially supported by the EU Horizon 2020 Project IPERION-HS (H2020-INFRAIA-2019-1, GA n. 871034), the Italian Project AMIS (Dipartimenti di Eccellenza 2018–2022, funded by MUR and Perugia University) and the EU - NextGenerationEU under the MUR National Innovation Ecosystem grant ECS00000041 - VITALITY. For the beamtime grants received, we thank ESRF-ID21 and ID13 beamlines (experiment n. HG-156, HG-159, and in-house beamtimes) and the ESRF-Historical materials BAG (experiments n. HG-172 and HG-213), implemented with support from the EU Horizon 2020 research and innovation programme under GA n. 870313, Streamline.

Acknowledgments

Authors acknowledge Loïc Huder and PaNOSC (EU Horizon 2020 Research and Innovation programme under GA n. 823852) for data analysis tools (Jupyter notebooks).

Supplemental Material

All supplemental material mentioned in the text is available in the online version of the journal.

References

1. T. Christiansen, M. Cotte, W. de Nolf, E. Mouro, et al. “Insights into the Composition of Ancient Egyptian Red and Black Inks on Papyri Achieved by Synchrotron-based Microanalyses”. *Proc. Natl. Acad. Sci. U. S. A.* 2020. 117(45): 27825–27835. 10.1073/pnas.2004534117.

2. A. Van Loon, J.J. Boon. “Characterization of the Deterioration of Bone Black in the 17th century Oranjezaal Paintings using Electron-Microscopic and Micro-Spectroscopic Imaging Techniques”. *Spectrochim. Acta, Part B*. 2004. 59(10-11): 1601–1609. 10.1016/j.sab.2004.03.021.

3. H. Béarat. “Les Pigments à Base de Plomb en Peinture Murale Romaine”. In: R. Pancella, editor. Preservation and Restoration of Cultural Heritage. Proceedings of the 1995 LCP Congress. Montreux, CH: École polytechnique fédérale de Lausanne, 24-29 September 1995. pp. 547–555.

4. C. Rémazeilles, E. Conforto. “A Buried Roman Bronze Inkwell: Chemical Interactions with Agricultural Fertilizers”. *Stud. Conserv.* 2008. 53(2): 110–117. 10.1179/sic.2008.53.2.110.

5. X. Zhang. “An Unusual Corrosion Product, Pyromorphite, from a Bronze An: a Technical Note”. *Stud. Conserv.* 2002. 47(1): 76–79. 10.1179/sic.2002.47.1.76.

6. S. Sotiropoulou, V. Perdikatsis, C. Apostolaki, A.G. Karydas, et al. “Lead Pigments and Related Tools at Akrotiri, Thera, Greece. Provenance and Application Techniques”. *J. Archaeol. Sci.* 2010. 37(8): 1830–1840. 10.1016/j.jas.2010.02.001.

7. Pliny the Elder. “Naturalis Historia”, 77 CE, https://www.perseus.tufts.edu/hopper/text?doc=Perseus%3Atext%3A1999.02.0137%3Abook%3D35%3Achapter%3D23 (accessed March 09 2024).

8. P. Holakooei, J.F. de Lapérouse, M. Rugiadi, F. Carò. “Early Islamic Pigments at Nishapur, North-eastern Iran: Studies on the Painted Fragments Preserved at The Metropolitan Museum of Art”. *Archaeol. Anthropol. Sci.* 2018. 10(1): 175–195. 10.1007/s12520-016-0347-7.

9. J. Winter. “Lead White in Japanese Paintings”. *Stud. Conserv.* 1981. 26(3): 89–101. 10.1179/sic.1981.26.3.89.

10. E. Mavropoulos, A. M. Rossi, A. M. Costa, C. A. C. Perez, et al. “Studies on the Mechanisms of Lead Immobilization by Hydroxyapatite”. *Environ. Sci. Technol.* 2002. 36(7): 1625–1629. 10.1021/es0155938.

11. P. Miretzky, A. Fernandez-Cirelli. “Phosphates for Pb Immobilization in Soils: a Review”. *Environ. Chem. Lett.* 2008. 6(3): 121–133. 10.1007/s10311-007-0133-y.

12. E. Mavropoulos, N. C. C. Rocha, J. C. Moreira, A. M. Rossi, G. A. Soares. “Characterization of Phase Evolution During Lead Immobilization by Synthetic Hydroxyapatite”. *Mater. Charact.* 2004. 53(1): 71–78. 10.1016/j.matchar.2004.08.002.

13. V. Laperche, S. J. Traina, P. Gaddam, T. J. Logan. “Chemical and Mineralogical Characterizations of Pb in a Contaminated Cail: Reactions with Synthetic Apatite”. *Environ. Sci Technol.* 1996. 30(11): 3321–3326. 10.1021/es960141u.

14. E. Sassoni. “Hydroxyapatite and Other Calcium Phosphates for the Conservation of Cultural Heritage: a Review”. *Materials*. 2018. 11(4). 10.3390/ma11040557.

15. Y. Zhu, B. Huang, Z. Zhu, H. Liu, et al. “Characterization, Dissolution and Solubility of the Hydroxypyromorphite-hydroxyapatite Solid Solution [$(Pb_xCa_{1-x})_5(PO_4)_3OH$] at 25 °C and pH 2-9”. *Geochem. Trans.* 2016. 17(1): 1–18. 10.1186/s12932-016-0034-8.

16. A. Fitch, C. Dejoie, E. Covacci, G. Confalonieri, et al. “ID22–the High-Resolution Powder-Diffraction Beamline at ESRF”, *J. Synchrotron Radiat.* 2023. 30(5): 1003-1012. 10.1107/S1600577523004915.

17. C. Riekel, M. Burghammer, R. Davies. “Progress in Micro- and Nano-diffraction at the ESRF ID13 Beamline”. *IOP Conf. Ser.: Mater. Sci. Eng.* 2010. 14(1): 012013. 10.1088/1757-899x/14/1/012013.

18. M. Cotte, V. Gonzalez, F. Vanmeert, L. Monico, et al. “The ‘Historical Materials BAG’: a New Facilitated Access to Synchrotron X-ray Diffraction Analyses for Cultural Heritage Materials at the European Synchrotron Radiation Facility”. *Molecules* 2022. 27(6). 10.3390/molecules27061997.

19. G. Ashiotis, A. Deschildre, Z. Nawaz, J.P. Wright, et al. “The Fast Azimuthal Integration Python Library: PyFAI”. *J. Appl. Crystallogr.* 2015. 48: 510–519. 10.1107/S1600576715004306.

20. L. Huder. “Jupyter notebooks for azimuthal integration”. 2021. https://gitlab.esrf.fr/loic.huder/juno (accessed March 09 2024).

21. M. Cotte, T. Fabris, G. Agostini, D. Motta Meira, et al. “Watching Kinetic Studies as Chemical Maps Using Open-Source Software”. *Anal. Chem.* 2016. 88(12): 6154–6160. 10.1021/acs.analchem.5b04819.

22. B.H. Toby. “EXPGUI, a Graphical User Interface for GSAS”. *Appl. Crystallogr.* 2001. (34): 210–213.

23. M. Cotte, E. Pouyet, M. Salomé, C. Rivard, et al. “The ID21 X-ray and Infrared Microscopy Beamline at the ESRF: Status and Recent Applications to Artistic Materials”. *J. Anal. At. Spectrom.* 2017. 32(3): 477–493. 10.1039/c6ja00356g.

24. S. Fisher, M. Oscarsson, W. De Nolf, M. Cotte, J. Meyer. “Daiquiri: a Web-based User Interface Framework for Beamline Control and Data Acquisition”. *J. Synchrotron Radiat.* 2021. 28(6): 1996–2002. 10.1107/S1600577521009851.

25. J. Rajendran, S. Gialanella, P.B. Aswath. “XANES Analysis of Dried and Calcined Bones”. *Mater. Sci. Eng., C* 2013. 33(7): 3968–3979. 10.1016/j.msec.2013.05.038.

26. R. A. Young, editor. The Rietveld Method, International Union of Crystallography. Oxford: University Press, 1995.

27. R.M. Wilson, J.C. Elliott, S.E.P. Dowker. “Rietveld Refinement of the Crystallographic Structure of Human Dental Enamel Apatites”. *Am. Mineral.* 1999. 84(9): 1406-1414. 10.2138/am-1999-0919.

28. A. Bigi, M. Gandolfi, M. Gazzano, A. Ripamonti, N. Roveri, S.A. Thomas. “Structural Modifications of Hydroxyapatite Induced by Lead Substitution for Calcium”. *J. Chem. Soc., Dalton Trans.*, 1991, 2883-2886. 10.1039/DT9910002883.

29. E.D. Ingall, J.A. Brandes, J.M. Diaz, M.D. De Jonge, et al. “Phosphorus K-edge XANES Spectroscopy of Mineral Standards”. *J. Synchrotron Radiat.* 2011. 18(2): 189–197. 10.1107/S0909049510045322.

30. L. C. Colocho Hurtarte, L. F. Souza-Filho, W. O. Santos, L. Vergütz, et al. “Optimization of Data Processing Minimizes Impact of Self-Absorption on Phosphorus Speciation Results by P K-edge XANES”. *Soil Syst.* 2019. 3(3): 1–13. 10.3390/soilsystems3030061.

31. V. Martin-Diaconescu, M. Gennari, B. Gerey, E. Tsui, et al. “Ca K-edge XAS as a Probe of Calcium Centers in Complex Systems”. *Inorg. Chem.* 2015. 54(4): 1283–1292. 10.1021/ic501991e.

32. S. Koutsopoulos. “Synthesis and Characterization of Hydroxyapatite Crystals: a Review Study on the Analytical Methods”. *J. Biomed. Mater. Res.* 2002. 62(4): 600–612. 10.1002/jbm.10280.

33. C. Rey, O. Marsan, C. Combes, C. Drouet, et al. “Characterization of Calcium Phosphates Using Vibrational Spectroscopies”. In: B. Ben-Nissan, editor. Advances in Calcium Phosphate Biomaterials. Berlin, Heidelberg: Springer Series in Biomaterials Science and Engineering, 2014. Vol. 2, pp. 229-266. 10.1007/978-3-642-53980-0_8.

34. H. Tsuda, J. Arends. “Raman Spectra of Human Dental Calculus.” *J. Dent. Res.* 1993. 72(12): 1609–1613. 10.1177/00220345930720121401.

35. G.R. Sauer, W.B. Zunic, J.R. Durig, R.E. Wuthier. “Fourier Transform Raman Spectroscopy of Synthetic and Biological Calcium Phosphates”. *Calcif. Tissue Int.* 1994. 54(5): 414–420. 10.1007/BF00305529.

36. W.P. Griffith. “Raman Studies on Rock-Forming Minerals. Part II. Minerals Containing MO_3, MO_4, and MO_6 Groups”. *J. Chem. Soc. A* 1970. (0): 286–291.

37. P.N. De Aza, C. Santos, A. Pazo, S. De Aza, et al. “Vibrational Properties of Calcium Phosphate Compounds. 1. Raman Spectrum of β-Tricalcium Phosphate”. *Chem. Mater.* 1997. 9(4): 912–915. 10.1021/cm960425d.

38. J.M. Stutman, J.D. Termine, A.S. Posner. “Vibrational Spectra and Structure of the Phosphate Ion in Some Calcium Phosphates.” *Trans. N. Y. Acad. Sci.* 1965. 27: 669–675. 10.1111/j.2164-0947.1965.tb02224.x.

39. J. Arends, J. Christoffersen, M.R. Christoffersen, H. Eckert, et al. “A Calcium Hydroxyapatite Precipitated from an Aqueous Solution. An International Multimethod Analysis.” *J. Cryst. Growth* 1987. 84(3): 515–532. 10.1016/0022-0248(87)90284-3.

40. D.C. O’Shea, M.L. Bartlett, R.A. Young. “Compositional Analysis of Apatites with Laser-Raman spectroscopy: (OH,F,Cl)apatites”. *Arch. Oral Biol.* 1974. 19(11): 995–1006. 10.1016/0003-9969(74)90086-7.

41. B.O. Fowler. “Infrared Studies of Apatites. I. Vibrational Assignments for Calcium, Strontium, and Barium Hydroxyapatites Utilizing Isotopic Substitution”. *Inorg. Chem.* 1974. 13(1): 194–207. 10.1021/ic50131a039.

42. W.E. Klee, G. Engel. “IR Spectra of the Phosphate Ions in Various Apatites”. *J. Inorg. Nucl. Chem.* 1970. 32(6): 1837–1843. 10.1016/0022-1902(70)80590-5.

43 S.J. Joris, C.H. Amberg. “The Nature of Deficiency in Nonstoichiometric Hydroxyapatites. I. Catalytic Activity of Calcium and Strontium Hydroxyapatites”. *J. Phys. Chem.* 1971. 75(20): 3167–3171. 10.1021/j100689a024.

44. H. Liu, X. Cui, X. Lu, X. Liu, et al. “Mechanism of Mn Incorporation into Hydroxyapatite: Insights from SR-XRD, Raman, XAS, and DFT Calculation”. *Chem. Geol.* 2021. 579: 120354. 10.1016/j.chemgeo.2021.120354.

45. A. Bigi, E. Boanini, C. Capuccini, M. Gazzano. “Strontium-substituted Hydroxyapatite Nanocrystals”. *Inorg. Chim. Acta* 2007. 360(3): 1009–1016. 10.1016/j.ica.2006.07.074.

46. Y. Jiang, Z. Yuan, J. Huang. “Substituted Hydroxyapatite: a Recent Development”. *Mater. Technol.* 2020. 35(11–12): 785–796. 10.1080/10667857.2019.1664096.

47. M. Li, X. Xiao, R. Liu, C. Chen, L. Huang. “Structural Characterization of Zinc-substituted Hydroxyapatite Prepared by Hydrothermal Method”. *J. Mater. Sci.: Mater. Med.* 2008. 19(2): 797–803. 10.1007/s10856-007-3213-4.

48. C. Miliani, F. Rosi, A. Daveri, B.G. Brunetti. “Reflection Infrared Spectroscopy for the Non-Invasive In Situ Study of Artists’ Pigments”. *Appl. Phys. A: Mater. Sci. Process* 2012. 106(2): 295–307. 10.1007/s00339-011-6708-2.

49. D. Buti, F. Rosi, B.G. Brunetti, C. Miliani. "In Situ Identification of Copper-based Green Pigments on Paintings and Manuscripts by Reflection FTIR." *Anal. Bioanal. Chem.* 2013. 405: 2699-2711. 10.1007/s00216-013-6707-6.

50. L. Monico, F. Rosi, C. Miliani, A. Daveri, B.G. Brunetti. "Non-Invasive Identification of Metal-oxalate Complexes on Polychrome Artwork Surfaces by Reflection Mid-Infrared Spectroscopy". *Spectrochim. Acta, Part A* 2013. 116: 270-280. 10.1016/j.saa.2013.06.084.

51. L. Monico, K. Janssens, C. Miliani, B.G. Brunetti, et al. “Degradation Process of Lead Chromate in Paintings by Vincent van Gogh Studied by Means of Spectromicroscopic Methods. 3. Synthesis, Characterization, and Detection of Different Crystal Forms of the Chrome Yellow Pigment”. *Anal. Chem.* 2013. 85 (2): 851–859. 10.1021/ac302158b.

52. F. Volpi, M. Vagnini, R. Vivani, M. Malagodi, G. Fiocco. “Non-Invasive Identification of Red and Yellow Oxide and Sulfide Pigments in Wall-Paintings with Portable ER-FTIR Spectroscopy”. *Journal of Cultural Heritage* 2023. 63: 158-168. 10.1016/j.culher.2023.07.019.

53. B.J. Reddy, R.L. Frost, S.J. Palmer. “A Near-Infrared Spectroscopic Study of the Phosphate Mineral Pyromorphite $Pb_5(PO_4)_3Cl$”. *Spectrochim. Acta, Part A* 2008. 71(2): 430–435. 10.1016/j.saa.2007.12.030.

54. F. Rosi, L. Cartechini, D. Sali, C. Miliani. “Recent Trends in the Application of Fourier Transform Infrared (FT-IR) Spectroscopy in Heritage Science: From Micro- to Non-invasive FT-IR”. *Phys. Sci. Rev.* 2019. 4(11): 20180006. 10.1515/psr-2018-0006.

55. C. Invernizzi, T. Rovetta, M. Licchelli, M. Malagodi. “Mid and Near-Infrared Reflection Spectral Database of Natural Organic Materials in the Cultural Heritage Field”. *Int. J. Anal. Chem.* 2018. 2018: 7823248. 10.1155/2018/7823248.

56. V. Gonzalez, M. Cotte, F. Vanmeert, W. de Nolf, K. Janssens. “X-ray Diffraction Mapping for Cultural Heritage Science: a Review of Experimental Configurations and Applications”. *Chem. - Eur. J.* 2020. 26(8): 1703–1719. 10.1002/chem.201903284.

57. F. Vanmeert, S. De Meyer, A. Gestels, E. A. Clerici, et al. “Non-invasive and Non-destructive Examination of Artists’ Pigments, Paints and Paintings by Means of X-Ray Imaging Methods”. In: M.P. Colombini, I. Degano, A. Nevin, editors. Analytical Chemistry for the Study of Paintings and the Detection of Forgeries. Springer International Publishing, Cham, 2022. pp. 317–357. 10.1007/978-3-030-86865-9_11.

58. S. Cersoy, P. Martinetto, P. Bordet, J.L. Hodeau, et al. “Identifying and Quantifying Amorphous and Crystalline Content in Complex Powdered Samples: Application to Archaeological Carbon Blacks”. *J. Appl. Crystallogr.* 2016. 49(2): 585–593. 10.1107/S1600576716003551.